

# Versatile magneto-optic Kerr effect polarimeter for studies of domain-wall dynamics in magnetic nanostructures

Corneliu Nistor, Geoffrey S. D. Beach, and James L. Erskine

*Department of Physics, The University of Texas at Austin, Austin, Texas 78712*

(Received 22 June 2006; accepted 27 August 2006; published online 2 October 2006)

This article describes a versatile instrument capable of probing magnetic domain-wall dynamics in microstructured thin films. The instrument combines a state-of-the-art scanning magneto-optic Kerr effect polarimeter that incorporates high-bandwidth signal detection, an integrated broadband magnet system, and a microwave probe station. Together, these subsystems enable a broad range of studies of field and current-driven domain-wall dynamics in submicrometer magnetic structures and devices. Domain-wall motion can be probed with  $\approx 2 \mu\text{m}$  spatial resolution and less than 2 ns temporal resolution. That motion can be driven by magnetic fields of up to  $\approx 100$  Oe amplitude with sinusoidal ( $>20$  MHz) or user-defined wave forms (20 ns rise time) or by electric currents from dc to  $\approx 10$  GHz. A detailed description of the instrument is provided as well as several experiments highlighting its capabilities, including hysteresis loop shape and magnetic energy loss measurements spanning ten decades of drive frequency; spatially and temporally resolved measurements of domain-wall propagation in submicrometer magnetic wires; and mobility measurements of field- and current-driven domain-wall motion. © 2006 American Institute of Physics.

[DOI: [10.1063/1.2356856](https://doi.org/10.1063/1.2356856)]

## I. INTRODUCTION

The magneto-optic Kerr effect (MOKE) has been widely used to probe the magnetic properties of ferromagnetic materials. A comprehensive review of the application of MOKE techniques to thin films was published in 1994 as part of a two-volume treatise<sup>1</sup> on ultrathin magnetic structures. The review<sup>2</sup> contains descriptions of mechanisms responsible for the magneto-optic response of ferromagnetic materials, macroscopic formulations of MOKE response in terms of the conductivity tensor, and a selection of MOKE experiments involving ultrathin films with extensive references.

The most recent applications of the MOKE as a tool for probing properties of ferromagnetic materials have begun to emphasize magneto-optical imaging of domain structure and high spatial and temporal resolution probes of spin dynamics in thin films and microstructures. A recent book<sup>3</sup> presents a comprehensive review of domain-wall phenomena and spin dynamics, including the applicable experimental methods available to observe and study spin distributions in ferromagnetic materials.

Several experimental approaches are available to probe spin dynamics of magnetic thin-film structures. One approach is based on inductive coupling. The availability of digital oscilloscopes having bandwidths exceeding 10 GHz (single sweep capture) and sampling bandwidths exceeding 100 GHz (repetitive sweep experiments) and fast pulse generators (pulse rise time below 100 ps) and photoconductive switches (rise times approaching 1 ps) offer one option for probing magnetization dynamics based on inductive detection of spin reversal in thin-film structures near a coplanar waveguide.<sup>4-6</sup> Recently reported temporal resolution of this technique is approximately 100 ps, but the ultimate resolution could approach 10 ps.

A second approach for probing spin dynamics is based on pulsed laser technology. The development and commercial availability of femtosecond lasers have created new opportunities for high-temporal-resolution studies of spin dynamics based on the MOKE. Pump-probe techniques<sup>7-15</sup> that utilize magneto-optical sampling and ultrashort current pulses produced by photoconductive switches<sup>7</sup> permit measurements of spin dynamics at diffraction-limited spatial resolution (1  $\mu\text{m}$ ) and at subpicosecond temporal resolution. These techniques applied to thin films and thin-film-based microstructures have been used to observe ferromagnetic resonance in the time domain,<sup>10</sup> measure spin damping parameters and magnetic relaxation<sup>9-12</sup> in microstructured samples, and image multimode magnetization reversal.<sup>11,12</sup> The technique has been extended to differentiate between surface and bulk spin excitations by detecting (surface sensitive) second-harmonic contributions<sup>13</sup> to MOKE signals. The addition of second-harmonic detection to a MOKE experiment offers the capability to simultaneously measure surface and bulk vector magnetization dynamics in magnetic thin films.<sup>14</sup> A recent review<sup>15</sup> covers many aspects of high-temporal-resolution imaging of spin distribution based on femtosecond laser technology.

A third approach for probing spin dynamics using MOKE techniques is based on continuous wave (cw) lasers. High temporal resolution is achieved by incorporating high-speed response in the drive-field magnet and in the polarimeter detection system. The laser-based approaches offer diffraction-limited spatial resolution and are capable of achieving higher sensitivity and spatial resolution than the inductive pick-up approach. This article describes a versatile cw-laser-based scanning MOKE polarimeter that achieves the high spatial ( $\approx 2 \mu\text{m}$ ) and temporal ( $\approx 1$  ns) resolutions

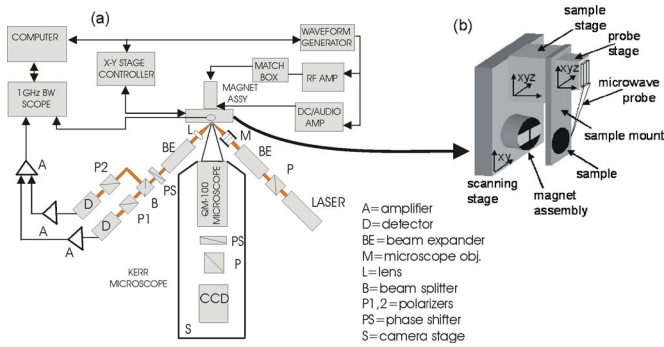


FIG. 1. MOKE instrument schematic and block diagram. Normal-incidence long-focal-length Kerr microscope ( $1 \mu\text{m}$  resolution) facilitates microstructure alignment at laser focus. Polarimeter is based on a cw-laser source incident at  $45^\circ$  from normal. Beam expander and microscope objective produce  $\approx 1 \mu\text{m}$  beam focus at sample. Magnet assembly is mounted on  $xy$  stage ( $1 \mu\text{m}$  accuracy with closed-loop optical encoders). Photomultiplier tubes with shortened dynode chains and 350 MHz amplifiers yield  $\approx 1$  ns response.

required to directly measure electric-current and field-driven domain-wall velocities and mobilities, and energy loss (hysteresis loops) in magnetic microstructures. The instrument also achieves the high sensitivity required to study Barkhausen phenomena in thin magnetic films and microstructures.

## II. HIGH-BANDWIDTH SCANNING MOKE POLARIMETER

The instrument, shown schematically in Fig. 1, combines a normal-incidence Kerr microscope with an oblique ( $45^\circ$ ) incidence high-bandwidth scanning MOKE polarimeter. The microscope, comprised of a long-focal-length (Questar) reflecting microscope coupled to a charge coupled device (CCD) camera (Princeton Research Pentamax), permits static imaging with  $1 \mu\text{m}$  resolution. The microscope is used for alignment of the sample and the magnet/probe station assembly and can also be used for static polar Kerr imaging of the sample. The polarimeter is based on a cw-laser source and includes optics that yield an adjustable-width Gaussian spot ranging from several millimeters down to a diffraction-limited size of  $\approx 2 \mu\text{m}$  in the sample plane. The sample is secured in a broadband magnet/microwave probe station assembly, which is mounted on a precision two-axis translation stage that permits computer-controlled scanning relative to the fixed laser spot with sub-100 nm precision. This section describes the various subsystems of the instrument.

### A. Polarimeter optics and MOKE detection

The instrument is set up on a commercial vibration isolation table (model TMC No. 784-491-02R). The polarimeter optics, configured as shown in Fig. 1(a), consist of standard off-the-shelf optical elements. The light source is a cw solid state laser (CrystalLaser RCL-658-50) with an operating wavelength of 658 nm and an output power of 45 mW. The output consists of a polarized single longitudinal mode (polarization ratio of 100:1) with high output power stability ( $<0.5\%$  over 24 h) and low intensity noise over a broad frequency range ( $<0.5\%$  from 10 Hz to  $>1$  GHz). Single-

mode operation is essential for the broadband measurements described later. The mode hopping inherent in standard (multimode) solid state and unstabilized gas lasers produces detrimental high-frequency amplitude modulations that complicate MOKE measurements at time scales shorter than  $1 \mu\text{s}$ .

The laser beam is polarized (polarizer extinction ratio  $<10^{-5}$ ), passes through a  $20\times$  beam expander, and is focused in the sample plane using a  $10\times$  microscope objective (Mitutoyo, [(numerical aperture) NA at 0.28]). The collection lens is a planoconvex lens with a NA of approximately 0.28 to match the microscope objective. Glan-Taylor polarizers are used for incident beam polarization and reflected beam analysis. The polarimeter can be configured to detect either component of in-plane vector magnetization by detecting the longitudinal MOKE (sensitive to magnetization in the plane of incidence) or the transverse MOKE (sensitive to magnetization perpendicular to the plane of incidence).<sup>2</sup> A polarization modulator (not shown) can be inserted between the incident polarizer and beam expander to rotate the incident polarization from  $p$  (parallel to plane of incidence) to  $s$  (perpendicular to plane of incidence) for in-plane vector magnetization measurements. All of the experiments described in this article utilized only  $s$  polarized light and therefore detect the longitudinal Kerr effect. In this case, the magnetization in the plane of incidence averaged over the focused light spot,  $\langle M_x \rangle$ , was detected.

For longitudinal MOKE detection, the analyzer is set at an angle  $\Phi_m$  from the plane of incidence. The MOKE (after phase shift compensation) introduces a rotation  $\Phi_K$  in the reflected light polarization that is proportional to  $\langle M_x \rangle$ . The transmitted intensity is governed by Malus' law, with  $\Phi = \Phi_m + \Phi_K$ ,

$$I(\Phi) = I_m \sin^2(\Phi) + I_0,$$

where  $I_m$  is the maximum transmitted intensity (analyzer aligned with the polarization axis,  $\Phi = \pi/2$ ) and  $I_0$  is the transmitted intensity at  $\Phi = 0$  due to residual depolarization of the beam and polarizer imperfections (finite extinction ratio). A quarter-wave plate is used to compensate elliptical polarization resulting from reflection by the sample to minimize  $I_0$ . In all cases of practical interest,  $I_0$  remains much larger than the Kerr signal (transmitted intensity change resulting from a Kerr rotation  $\Phi_K$ ). Therefore, differential detection (or use of an offset voltage) is necessary to exploit the full dynamic range of the analog-to-digital (A/D) device used to measure and record the signal. Differential detection was implemented by placing a nonpolarizing beam splitter after the quarter-wave plate to divide the reflected beam into two beams. Analyzers on these two beams were set at  $+\Phi_m$  and  $-\Phi_m$ , respectively, from the null. The intensity  $I(\Phi)$  is an even function of  $\Phi$ , but  $dI/d\Phi = 2I_m \sin \Phi \cos \Phi$  is an odd function. With  $\Phi = \Phi_K + \Phi_m$  and  $\Phi = \Phi_K - \Phi_m$  for the Kerr rotation and offset angles for the two beams, the differential signal is given by

$$\text{Signal} \propto \alpha I_m \sin 2\Phi_m \sin 2\Phi_K.$$

With reasonably balanced detection of the two beams (same  $\Phi_m$  and same detector gain), this differential detection strategy allows the full dynamic range of the detection electron-

ics to be utilized, while minimizing fluctuations and drifts resulting from laser intensity changes and some sources of microphonic noise. Optimization of  $\Phi_m$  is discussed in Sec. II D.

## B. Mechanical configuration

Several mechanical translation stages illustrated in Fig. 1(b) are required to align the various components and operate the system. The magnet assembly, sample, and microwave probe are mounted together on a large open-frame two-axis translation stage (Daedal 800 000 series) that is rigidly mounted vertically on the optical table. This scanning stage translates the sample in the common focal plane of the camera and polarimeter. It is used in *scanning mode* to move the sample laterally relative to the polarimeter laser spot while keeping it fixed with respect to the magnet and microwave probe. The magnet assembly is fixed to the scanning stage, and a three-axis stage (*sample stage*) mounted to the scanning stage is used to align the sample at the magnet wire (see Sec. II E). Finally, a three-axis stage (*probe stage*) mounted on the sample stage is used to align the microwave probe with respect to the sample and land the probe on the sample surface contact pads.

The normal-incidence microscope/CCD camera is used to facilitate alignment. In order to keep the sample in focus and in the camera field of view during and after alignment, the camera/microscope assembly is mounted on a separate two-axis translation stage (*camera stage*) fixed to the optical table. This stage allows motion in the polarimeter plane of incidence. Finally, the polarimeter microscope objective, used to focus the polarimeter laser on the sample, is mounted on a high-stability three-axis flexure stage (*objective stage*) fixed to the optical table. This stage is used to align the objective with the laser beam axis and adjust its focus on the sample.

The sample stage, probe stage and objective stage are commercial manual stages with submicrometer adjustment precision. The camera stage is a custom-built manual-drive stage with 10  $\mu\text{m}$  precision in both axes. The scanning stage, a commercial stepper-motor-driven stage, is described further in the following subsection.

## C. Scanning mode operation: Mechanical and optical resolutions

The spatial resolution of the scanning polarimeter is defined by the spatial profile of the laser spot and the precision with which the spot can be located on a sample. The laser is incident on the sample at 45°, resulting in an elliptical Gaussian profile with a long axis (in the plane of incidence)  $\sqrt{2}$  times wider than the short axis. The spot profile is determined, and its width optimized for each experiment, by using a cleaved edge of the substrate [single-crystalline Si(100) in all of our work] as a “knife edge,” as shown in Fig. 2. The substrate edge is scanned across the spot and the reflected intensity recorded. The result for an optimally focused spot is shown in Fig. 2(b) and is well fitted by an error function representing the integrated intensity of the reflected portion of the Gaussian beam. The full width at 1/e intensity of the

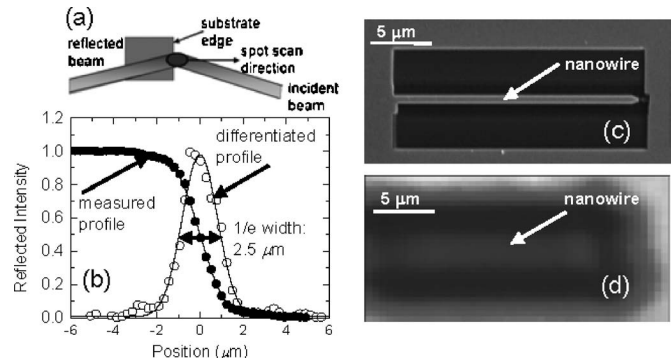


FIG. 2. (a) Schematic of knife-edge measurement of beam profile. (b) Reflected beam intensity profile as the optimally focused laser spot is scanned over the cleaved edge of a Si substrate (solid symbols), along with numerically differentiated intensity profile (open symbols). The solid lines are fits to an error function profile and a Gaussian profile. (c) Plan-view scanning electron micrograph of a  $20 \times 0.6 \mu\text{m}^2$  Permalloy nanowire, milled from a continuous film of Permalloy. Regions of light contrast correspond to unmilled regions of the metal layer. (d) Kerr susceptibility map of the same nanowire, presented with the same spatial scale as in (c). Lighter contrast corresponds to higher magnetic signal.

corresponding Gaussian is 2.5  $\mu\text{m}$  along the long axis, consistent with the diffraction-limited width expected for the optical components used. The spot size can be varied from this minimum to several millimeters in diameter by defocusing the objective, thus permitting the magnetization to be probed over length scales spanning several orders of magnitude.

The relatively high laser power (approximately 50 mW) and small spot size ( $\approx 2 \mu\text{m}$ ) result in a fairly high-power density of  $10^{10} \text{ W/m}^2$  at the sample. The high laser power density is essential in order to achieve good signal-to-noise ratio in MOKE measurements of magnetic response of microstructures, but could result in undesirable local heating. The temperature increase resulting from local power dissipation in a metallic sample is given by

$$\Delta T = \frac{3P_{\text{abs}}}{\pi\lambda_{\text{th}}d_{\text{sp}}},$$

where  $P_{\text{abs}}$  is the laser power absorbed,  $\lambda_{\text{th}}$  is the thermal conductivity of the sample, and  $d_{\text{sp}}$  is the beam diameter. For typical values in experiments reported in this article,  $\Delta T$  is estimated to be of the order of 1 K and verified by monitoring the resistance of nanowires illuminated by the polarimeter laser.

The scanning stage, on which the magnet/probe assembly and sample are mounted, is an open-frame two-axis commercial stepper-motor-driven stage. This stage is used to scan the sample relative to the focused polarimeter beam. The stepper motor drives include optical position sensors that permit closed-loop computer control of the sample position at the polarimeter/microscope focus to 0.5  $\mu\text{m}$  resolution and 1  $\mu\text{m}$  absolute accuracy. The stepper motors and lead screws yield a lower limit  $x$ - $y$  stage step size of 20 nm and routinely permit repetitive raster scans with sub-100 nm precision. Unidirectional raster scanning is implemented to avoid backlash effects that would occur in bidirectional scanning.

In preparation for an experiment, the magnetic structure is positioned in the focused laser spot using the normal-incidence microscope to view diffuse scattering from the sample. The structure is then scanned across the spot (by translating the scanning stage relative to the fixed spot location) to precisely locate the measurement region of interest (typically a microfabricated planar structure) by generating a magnetic “susceptibility map.”<sup>16</sup> Figure 2(c) shows a plan-view scanning electron micrograph of a  $\text{Ni}_{80}\text{Fe}_{20}$  stripe 600 nm wide and 20  $\mu\text{m}$  long. The stripe was fabricated using focused ion beam milling and is separated from the continuous film on each side by a 4- $\mu\text{m}$ -wide trench. The susceptibility map was generated by applying a 10 kHz square-wave magnetic field with an amplitude sufficient to simultaneously reverse magnetization of both the film and the stripe. A lock-in amplifier tuned to the magnetic-field drive frequency was used to record the MOKE signal while raster scanning the sample on a two-dimensional (2D) grid. The image corresponds to a two-dimensional map of the magnetic susceptibility. The submicrometer magnetic stripe is clearly resolved in this image, and structural features can be repeatedly identified from image cross-sectional slices with better than 100 nm precision.

#### D. High-bandwidth signal detection

The choice of detectors is determined by the type of experiment to be carried out. Experiments that explore Barkhausen effects<sup>17</sup> (stochastic motion of domain walls) require the highest achievable MOKE sensitivity because signal averaging is not possible. The highest sensitivity is achieved by using detectors that yield the highest quantum efficiency at the source wavelength. Standard silicon detectors achieve nearly unity quantum efficiency for visible wavelengths. The intrinsic noise of solid state detectors scales with detector area, but a small-area (1 mm)<sup>2</sup> silicon detector coupled to a low noise preamplifier can deliver shot-noise limited signal-to-noise ratios under typical conditions encountered in MOKE polarimetry. Small-area silicon detectors deliver 1 ns response (50  $\Omega$  load) but gain-bandwidth products of currently available low-noise preamplifiers limit the practical response to about 200 ns when a 1 k $\Omega$  load resistor is used with a 1 MHz bandwidth low-noise amplifier.

Experiments that explored Barkhausen effects<sup>17</sup> used small-area silicon detectors (New Focus model No. 1621) coupled to a low-noise wide-band dc differential amplifier (Stanford Research Systems model No. 560). A 1 k $\Omega$  load was used to increase the detected voltage without significantly reducing the system rise time, which was primarily limited by the preamplifier bandwidth. The output signal from the differential amplifier was digitized and processed as described later.

High-speed detection is possible in experiments that allow signal averaging. These experiments include energy loss measurements [ $H_c^*(\omega)$ ], hysteresis loop shape measurements, and domain-wall dynamics measurements in systems with repetitive excitation. In these experiments, photomultiplier tubes and wide-band amplifiers are required. The quantum efficiency of photomultiplier tubes is low (about 10% for wavelengths near 658 nm), but the high speed (below

1 ns rise time) and high gain ( $>10^5$ ) of photomultiplier tubes result in modest gain-bandwidth requirements for the preamplifiers. Experiments that required high speed were carried out using photomultiplier tubes (Hamamatsu model R1894). In order to achieve fast response (0.8 ns rise time), shortened dynode chains (reduced from eight to four stages) were used in both channels. Gain drift was reduced by using the same high-voltage supply for both tubes. Wide-band dc amplifiers were used: two cascaded ( $5\times$  voltage gain) stages of 350 MHz dc coupled amplifiers (Stanford Research Systems Model SIM914) for each channel. The preamplifier outputs were processed by a LeCroy 500 MHz differential amplifier probe and digitized by a four-channel, 8 bit (1 GHz bandwidth) digital oscilloscope (LeCroy Wavepro 960).

The polarimeter setting  $\pm\Phi_m$  required to obtain optimum signal-to-noise ratio response is dependent on the detectors and front-end electronics used, which depends on the sensitivity and bandwidth requirements just described. For silicon detectors and (bandwidth-limited) low-noise amplifiers, the detection system can achieve the shot noise limit where the noise is dominated by statistical fluctuations in detected intensity resulting from the discrete nature of detected photon flux ( $N$  photons/s). In this “shot-noise limit,” the detected signal is proportional to  $N$  and noise is proportional to  $\sqrt{N}$ . A straightforward analysis reveals that the optimum analyzer settings  $\pm\phi_m$  are governed by the ratio  $I_0/I$ , which is related to the system extinction ratio  $\epsilon$ . Typical values for  $\phi_m$  in this limit are a few degrees. High-speed operation requires wide amplifier bandwidth, and assuming that mechanical noise, laser fluctuations and rf coupling can be eliminated, the fundamental noise limit is amplifier Johnson noise given by  $N_J = \sqrt{4\kappa\text{TRB}}$  where (in the specific case described here)  $R = 50 \Omega$  for amplifier impedance match and  $B = 350 \text{ MHz}$  is the amplifier bandwidth. At room temperature, the preamplifiers yield Johnson noise equivalent to about 20  $\mu\text{V}$  across 50  $\Omega$ . Under typical operating conditions for our polarimeter using photomultiplier detectors and the 45 mW solid state laser, an estimate of the shot noise across the 50  $\Omega$  load yields about 2  $\mu\text{V}$ ; therefore the signal-to-noise ratio is limited by amplifier Johnson noise (independent of  $N$ ). In this case, the signal-to-noise ratio is optimized by simply maximizing the signal, which occurs when  $\sin(2\phi_m) = 1$  or  $\phi = 45^\circ$ . These optimum polarizer settings (for both shot-noise-limited and Johnson-noise limited detection) have been verified empirically in numerous experiments.

#### E. Broadband magnet system

The broadband magnet is shown schematically in Figs. 3(a) and 3(b). The field is generated by passing a high current through a short (4 mm) 500- $\mu\text{m}$ -wide copper wire of semicircular cross section soldered between  $\frac{1}{4}$ -in.-diameter copper electrodes. Field maps [Figs. 3(c) and 3(d)] were calculated to characterize the magnetic field in the sample plane and along a line perpendicular to it. The substrate is placed directly against the wire, and the Oersted field generated by the current provides a field in the substrate plane. In order to maximize the field amplitude at the substrate surface, the substrate thickness is kept to a minimum; all of the magnetic

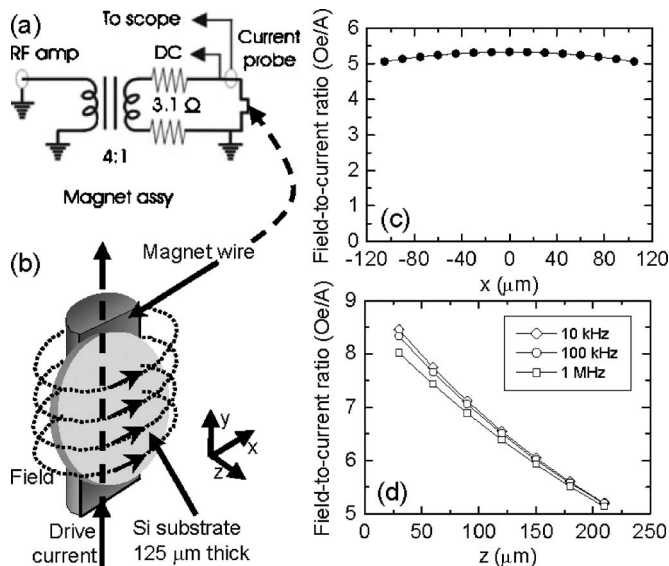


FIG. 3. Broadband magnet schematic and frequency characteristics. (a) Circuit diagram of the magnet design. The load resistors in the secondary circuit are absent in the high-frequency version. (b) Schematic of substrate orientation near the magnet wire (substrate not drawn to scale). [(c) and (d)] Calculated field amplitudes for the magnet wire vs position, including skin effects for several frequencies. Axes are defined by the schematic in (b).

films used in our studies were deposited on 125- $\mu\text{m}$ -thick high-resistivity Si wafers. At this wire-sample separation, the in-plane field is  $\approx 6$  Oe/A.

Two interchangeable broadband magnet systems are currently in use in this instrument. One is capable of dc operation and has a high-frequency cutoff of  $\approx 1$  MHz. The second sacrifices low-frequency capability to extend the high-frequency cutoff beyond 20 MHz. Both systems are built around ferrite-core rf transformers that couple the magnet wires to the rf power supply with a 4:1 turn ratio, yielding a 16:1 impedance ratio. The dc-capable version includes a bank of carbon resistors in the secondary winding (magnet side) to produce a 50  $\Omega$  primary input load with low inductive reactance suitable for the rf amplifier. An added advantage of the resistor bank is that dc and audio-drive currents can be applied directly to the magnet wire, with the load resistors serving to isolate the transformer [Fig. 3(a)]. In the second magnet system, the resistive load in the secondary is eliminated and the loop shortened to lower the inductance, increasing the operating frequency.

The magnetic field is monitored by measuring the current in the magnet wire; calibration of the magnet current/field ratio is discussed below. In the dc-capable version, standard active scope current probes are used to monitor low-frequency currents applied directly to the magnet wire [dc input in Fig. 3(a)]. High-frequency currents are measured using a 200 MHz bandwidth passive inductive current probe incorporated into the single-turn secondary (Pearson model 2877). As seen in Fig. 4, this probe faithfully reproduces the fastest rise time currents produced in the magnet.

Three high-power amplifiers with overlapping frequency ranges are used to drive the magnet(s). A Kepco BOP20-20-M (dc-10 KHz) bipolar supply and McIntosh 352 audio amplifier (20 Hz–200 KHz) are used for applying low-

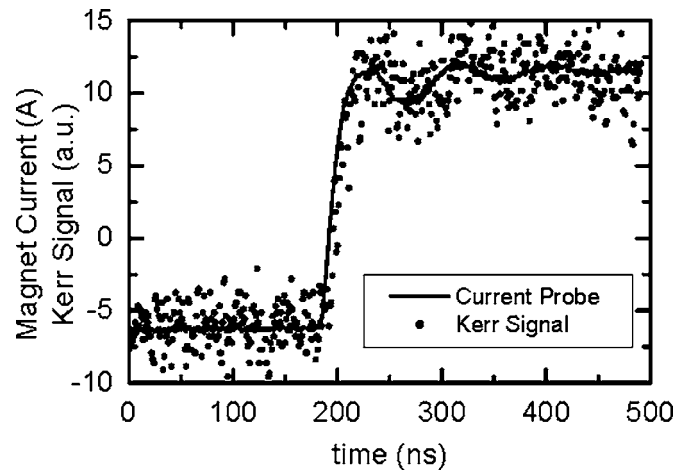


FIG. 4. Measured current in the broadband magnet wire (solid line) and Kerr rotation measured in the phase calibration line (symbols) after the application of a current step wave form. The field wave form, proportional to the Kerr signal, closely follows the current wave form, indicating that the measured current wave form accurately characterizes the field wave form subjected to the sample. The temporal shift between the two is used to characterize the phase shift between the two measurement channels.

frequency currents of up to 20 A directly to the magnet wire of the dc-capable magnet assembly. High-frequency currents are obtained by driving the magnet primary with an Amplifier Research (model 150A-100B) 150 W rf amplifier. This amplifier is designed to deliver its full power to the load independent of mismatch and is able to generate currents in the magnet secondary of up to  $\approx 20$  A. In all cases a dc to 30 MHz function generator (Stanford Research Systems DS345) was used to supply the input wave form to the power amplifier.

In addition to the integrated broadband magnet system, the instrument includes a standard Helmholtz magnet that can be used to provide a dc field bias or to generate low-frequency ac magnetic fields. The current/field ratio at the surface of a mounted sample is obtained by measuring a magnetic hysteresis loop (with MOKE) using the broadband magnet wire and observing the shift in that loop caused by a (calibrated) dc bias field generated by the coil magnet. These measurements agree with the field calculated by numerically integrating the Biot-Savart law over the wire cross section. Figures 3(c) and 3(d) show calculations of the field/current ratio calculated as a function of distance from the wire and position across the width of the wire. The field is found to be uniform to within 5% over a distance of 200  $\mu\text{m}$ . Hence, microfabricated planar structures with lateral dimensions of up to several hundreds of micrometers can be driven by relatively uniform in-plane fields. Over this same region, the field component normal to the film is below 1.25 Oe/A.

For high-frequency drive currents, the skin effect leads to a nonuniform current distribution in the magnet wire. The field calculations, described above, have therefore been carried out in two limits: a low-frequency limit in which the current distribution is uniform over the wire cross section, and a high-frequency limit in which the current is confined to a surface layer (skin depth  $\delta \propto 1/f$ ). Figure 3(d) shows that even at the highest frequencies of interest, at which the skin depth is small compared to the wire radius  $r_0$  ( $r_0/\delta \approx 7.5$  for

Cu at  $f=1$  MHz), the field amplitude at the sample surface is not a strong function of  $\delta$ .

The frequency response of the broadband magnet system has been characterized by measuring the magnet current amplitude versus frequency for a fixed-amplitude sinusoidal drive at the rf amplifier input. Current-frequency characteristics are shown in Fig. 5(a) for the high-frequency magnet system (lacking the secondary resistor bank) at two input amplitudes. The response is approximately linear over this range, and the current amplitude begins to roll off above 10 MHz, with a 3 dB point of  $\approx 23$  MHz. The high-frequency 3 dB points of the Pearson current probe and the rf power amplifier are 200 and 100 MHz, respectively. Therefore, although the data in Fig. 5(a) characterize the full magnet/amplifier/probe system, the frequency characteristic is dominated by the magnet.

The high bandwidth of the magnet system enables the generation of a broad range of drive-field wave forms, as seen in Figs. 5(b)–5(d). This capability has contributed to the ability of this instrument to probe a wide array of domain-wall dynamics. Hysteresis loop measurements require a linear ramp or sinusoidal drive field. Large-amplitude sinusoidal-field wave forms are routinely generated using this magnet system spanning frequencies from the millihertz range to the megahertz range.

Time-of-flight measurements of domain-wall velocities require the application of fast-rise-time field steps. The step response of the high-bandwidth magnet is shown in Fig. 5(c) and occurs with a 10%–90% rise time of about 25 ns. The response is accompanied by substantial ringing ( $\approx 12\%$ ) and signal droop beyond  $1 \mu\text{s}$ . The digital signal generator used here is capable of outputting pointwise-defined arbitrary wave forms with 25 ns time resolution and can be used to generate a compensating drive signal to achieve nearly ideal step response. By iteratively tuning the input wave form, overshoot and ringing in the step wave form generated with a compensated drive can be reduced to below 2%, as seen in Fig. 5(c), while adding only about 10 ns to the rise time.

The broadband magnet system driven by user-defined input wave forms is also capable of generating more complex field sequences that can be used to precisely manipulate domain walls in magnetic structures. Wave form shaping has been used, for example, to inject domain walls into magnetic nanowires prior to measuring low-field propagation. Figure 5(d) shows a single field pulse, with a full width at half maximum (FWHM) of 45 ns, generated by the magnet. Such a pulse can controllably displace a domain wall by several micrometers depending on its amplitude.

## F. Microwave probe assembly and device structures

The ability of spin-polarized electric current to drive magnetic domain-wall motion via “spin torque” has been recognized for several years.<sup>18–21</sup> The system described in this article is ideally suited to explore the dynamics of the spin-torque interaction. Typical experiments in current-driven domain-wall motion involve ferromagnetic stripes or nanowires. Such magnetic wires restrict domain-wall motion to occur along the wire axis and facilitate the injection of current through a domain wall. Device structures in the stud-

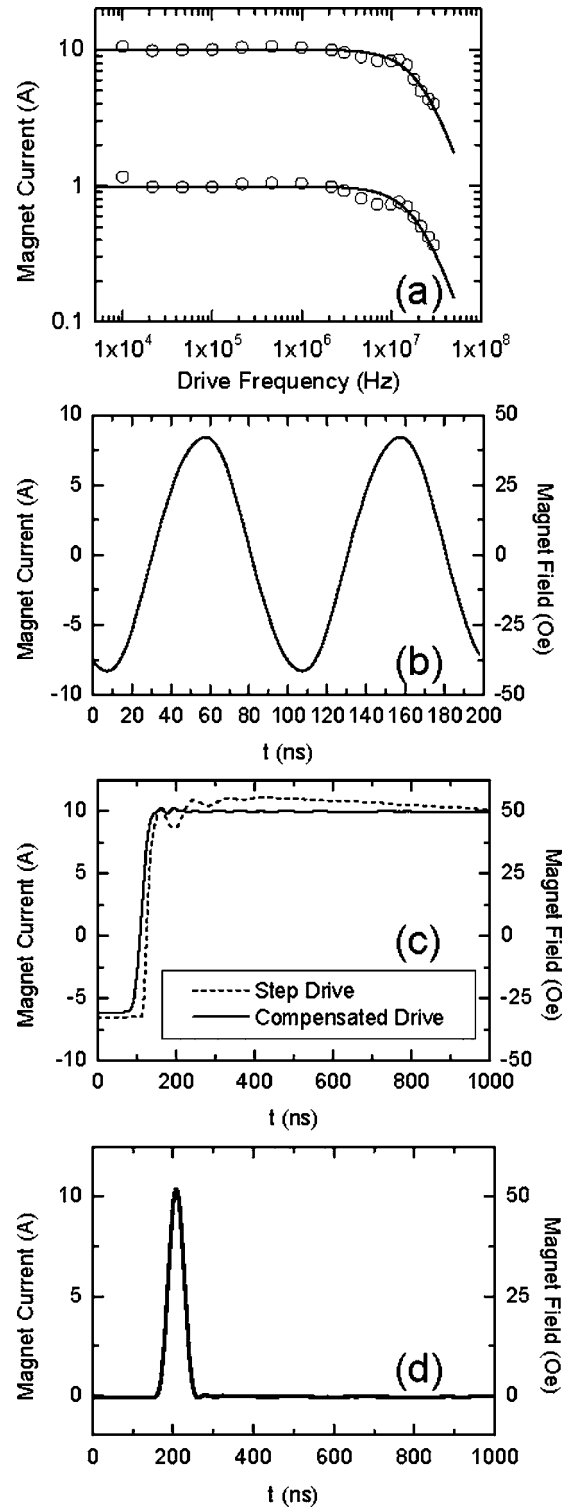


FIG. 5. (a) Measured magnet current (high-frequency version) as a function of frequency for sinusoidal input drives of two fixed amplitudes. The current –3 dB point occurs at approximately 23 MHz. (b)–(d) show various examples of current/field wave forms produced in the magnet wire. (b) 10 MHz sinusoid. (c) Magnet current in response to a square-wave input (step) and a compensated step wave form (see text). (d) Magnet current pulse with a FWHM of 45 ns.

ies described here were fabricated from continuous  $\text{Ni}_{80}\text{Fe}_{20}$  films deposited on thermally oxidized Si(100) wafers (with a 30 nm thermal oxide layer). Typical wire dimensions are 20 nm thick and  $40 \mu\text{m}$  long, with widths of several hun-

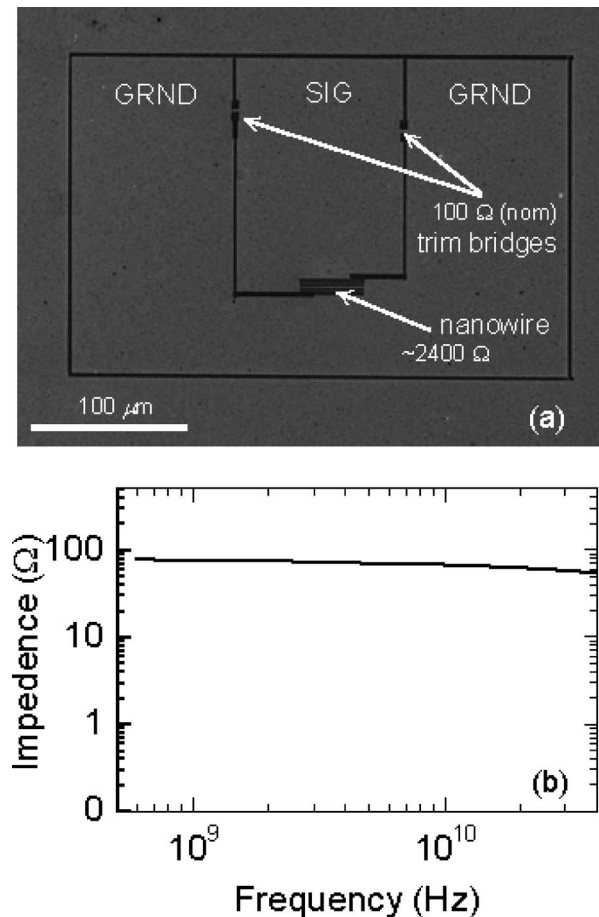


FIG. 6. (a) Plan-view scanning electron micrograph of device structure designed for driving ferromagnetic nanowire with microwave currents. Regions of light contrast correspond to the unmilled metal regions. (b) Device impedance measured from 500 MHz to 40 GHz.

dreds of nanometers, yielding resistances of several kilohms.

The sample translation assembly incorporates a dc–40 GHz microwave probe with a 100- $\mu\text{m}$ -pitch ground-signal-ground configuration (Cascade Microtech Infinity Probe model J40-GSG-100). The probe is mounted on a three-axis precision stage that is fixed to the sample stage (see Fig. 1). The normal-incidence high-resolution microscope and CCD camera are used to position the probe and land it on lithographically defined contact pads that permit application of electric current to a suitably designed structure. The application of dc is achieved using a constant current source (Keithley 2400) that permits simultaneous resistance measurements to monitor Joule heating. High-frequency instrumentation available for use with the polarimeter includes a fast pulse generator with 150 ps rise time, 0.2–2 ns duration bipolar pulses of up to 20 V (Avtech model AVP-AV-HV3-B-UTXB), and a cw signal generator (dc to 1 GHz, Rhodes and Schwartz model SML01).

Device design for dc studies is relatively straightforward. The nanowire device includes two large-area pads at its ends to permit dc injection. The application of high-frequency (microwave) current excitations to a nanowire structure requires more attention to device design. A device structure suitable for probing ac-induced dynamics over an excitation bandwidth of over 10 GHz is shown in Fig. 6.

Figure 6(a) displays a plan-view scanning electron microscopy (SEM) image of a ground-signal-ground configuration  $\text{Ni}_{80}\text{Fe}_{20}$  device structure engineered to permit both magnetic-field and broadband electric-current manipulation of domain walls in a model one-dimensional (1D) magnetic system. The nanowire under study spans a milled trench separating the signal pad from the dual ground pads. The device incorporates symmetrically arranged nominally 100  $\Omega$  trim bridges (with resistance tuned by controlling wire dimensions) in parallel with each other and with the nanowire (with a much larger resistance of several kilohms). These bridges are designed to yield a 50  $\Omega$  probe input termination.

The device performance has been characterized using a separate microwave probe station (with a probe identical to that in the polarimeter) and a 500 MHz–40 GHz network analyzer (HP 8510B). The response (device and probe impedance), shown in Fig. 6(b), is relatively flat to over 10 GHz demonstrating that device capacitance can be neglected in fast pulse measurements (approximately 100 ps rise time). The nanowire inductance and the loop inductance of the circuit ( $<0.1$  nH) are negligible at 10 GHz compared with the several kilohms of the nanowire device. Therefore the current through the nanowire can be calculated directly from the voltage applied to the probe. For a 20 V pulse, the current through a 600-nm-wide nanowire is approximately 8 mA yielding a current density of  $7 \times 10^{11}$  A/m<sup>2</sup>, within the range necessary to impart significant velocity to a domain wall via the spin-torque interaction.<sup>22</sup>

### G. System operation and control

The polarimeter is controlled by a fully integrated menu-driven software system written in LABVIEW. The scanning stage motors are operated over an RS232 interface and the remaining instrumentation (oscilloscope, function generator, current source, etc.) are controlled via an IEEE488 bus. The software enables centralized instrument configuration and has built-in interactive routines for stage motion, 1D and 2D magnetic and topographic (reflectivity) mapping and centering, user-defined drive-field wave form editing, automated-measurement routine scripting, and postmeasurement data analysis.

High-bandwidth measurements require signal averaging of a repetitive wave form to obtain requisite signal-to-noise ratios. In this instrument, the amplified Kerr signal from a Permalloy thin film that fully intercepts the laser spot has a magnitude of about 1 mV, whereas the amplifier noise at the full system bandwidth is about 20 mV at the scope input. Achieving a signal-to-noise ratio of 10 requires averaging of  $\approx 4 \times 10^4$  repetitively measured wave forms. Measurements consist of applying a repetitive drive wave form to the magnet and using a transistor-transistor logic (TTL) output trigger signal from the digital function generator to trigger oscilloscope acquisition at the beginning of each wave form. The trigger jitter of these instruments is far less than the 2 ns temporal resolution of the polarimeter. A deep oscilloscope memory is exploited to store and subsequently average on-board a sequence of measured wave forms, transferring only the final averaged wave form over the IEEE488 bus. At 500

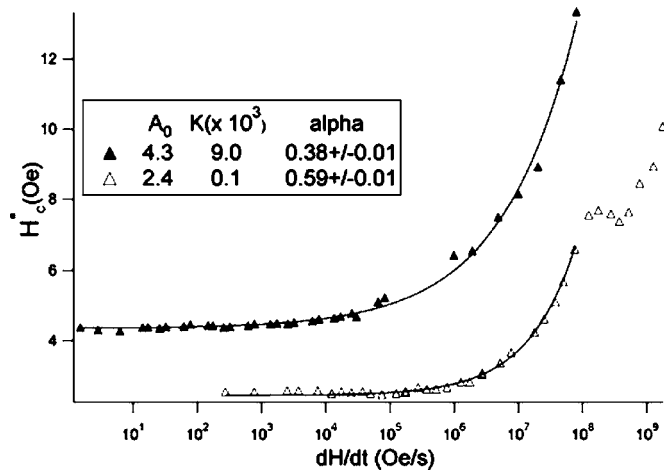


FIG. 7. Dynamic coercive force  $H_c^*(\omega)$  measured for two thin Permalloy films over 10 decades in drive frequency, showing frequency-dependent scaling behavior.

points per wave form in a  $4 \times 10^4$  wave form sequence, approximately 15 s is necessary to acquire, average, and transfer the data to the personal computer (PC).

### III. MEASUREMENTS OF DOMAIN-WALL DYNAMICS USING HIGH-BANDWIDTH SCANNING MOKE

The instrument described in Sec. II has been in operation for over two years. This section describes several selected experimental results that document the capabilities of the instrument.

#### A. Hysteresis loop shape and energy loss scaling measurements

The polarimeter is capable of measuring spatially resolved hysteresis loops. The area enclosed by an  $M(H)$  (hysteresis) loop is proportional to the (local) magnetic energy dissipation per cycle. Detailed analysis<sup>23</sup> of hysteresis loops in terms of domain-wall motion based on a mobility relationship

$$v(H) = \xi(H - H_c)^\alpha \quad (1)$$

reveals that specific features of the hysteresis loop shape can be used to obtain information about the mobility equation parameters—the mobility  $\xi$ , the power-law exponent  $\alpha$ , and the dynamic coercive field  $H_c$ . Eddy-current damping of domain-wall motion is suppressed in thin-film samples due to thickness dependent scaling,<sup>24</sup> therefore, measurements of spatially resolved frequency-dependent hysteresis loop shapes and loop areas in thin-film structures provide information on local spin damping mechanisms and local energy dissipation.

Magnetic energy loss scaling measurements carried out using the polarimeter described in this article have clarified the understanding of magnetic-loss scaling phenomena.<sup>25</sup> The high-speed response of the polarimeter permits meaningful measurements of loop shapes and loop areas over a wide range of frequencies (over 10 decades), as shown in Fig. 7. The high spatial resolution allowed scaling measurements to be carried out on microstructures of various shapes

and sizes that revealed the role static coercivity effects played in the scaling behavior. These measurements have shown that the energy loss [which is proportional to the dynamic coercivity  $H_c^*(\omega)$  in square-loop samples] can be fitted to a universal scaling function

$$H_c^*(\omega) = H_{dp} + A \left( \frac{dH}{dt} \right)^\beta, \quad (2)$$

where  $H_{dp}$  is a static depinning field and  $A$  and  $\beta$  are fitting parameters. Under very general assumptions related to domain-wall dynamics, it can be shown that  $\beta = 1/(1+\alpha)$ , implying that loss scaling measurements permit characterization of the mobility equation.

The polarimeter frequency range is broad enough to follow the scaling described by the mobility equation to a frequency where the model is no longer valid<sup>26</sup> (Fig. 7).

Meaningful determination of the scaling exponent  $\beta$  by fitting measured values of  $H_c^*(\omega)$  to the scaling function [Eq. (2)] requires accurate accounting of electronic phase shifts in the MOKE polarimeter. A measured phase shift between the drive-field current and detected change in magnetization can result from an intrinsic magnetic response or from the detection electronics time delays and electronic phase shifts. The detection electronics phase shift can be accurately measured at a given drive-field frequency by replacing the ferromagnetic sample with a Faraday rotation device. Our calibrations are based on a special glass cube of MOS-04 having a high Verdet constant  $V = 87$  rad/T m. With an effective path length of 1 mm, a Faraday rotation of  $\Phi \approx 0.5$  mrad is achieved. The signal from this rotation can be averaged to a high signal-to-noise ratio and used to obtain an accurate measure of instrument contributions to the phase shift.

Instrument phase shifts are negligible at frequencies below several hundreds of kilohertz. Phase shifts resulting from the Pearson current probe can be modeled based on a single pole filter response having a corner frequency at the upper cutoff frequency  $f_c = 200$  MHz (electronic phase shift  $\approx 45^\circ$  at  $f_c$ ). Similarly, large phase shifts occur in the wide-band amplifiers near their upper cutoff frequencies ( $f_c \approx 350$  MHz), and photomultiplier tube transit times ( $\tau \approx 15$  ns) and cable delay transit times ( $\tau \approx 1$  ns/ft) can also be measured separately. However, the best approach to obtain accurate values of  $H_c^*(\omega)$  is to perform an accurate phase shift calibration at each drive-field frequency using a Faraday cell.

#### B. Time-of-flight measurements: Domain-wall velocities and mobilities

The MOKE instrument described in this article can be used to carry out time-of-flight measurements of domain-wall propagation in model one-dimensional microstructures. This measurement can be viewed as a modern micron-scale version of the classic Sixtus-Tonks experiment<sup>27</sup> that used pick-up coils to determine propagation velocities of domain walls in ferromagnetic wires.

Figure 8 illustrates a typical set of time-of-flight data for a domain wall propagated in a  $600\text{-}\mu\text{m}$ -wide thin-film Permalloy nanowire. A field step is applied to nucleate a domain wall in the magnetically soft continuous film and to inject

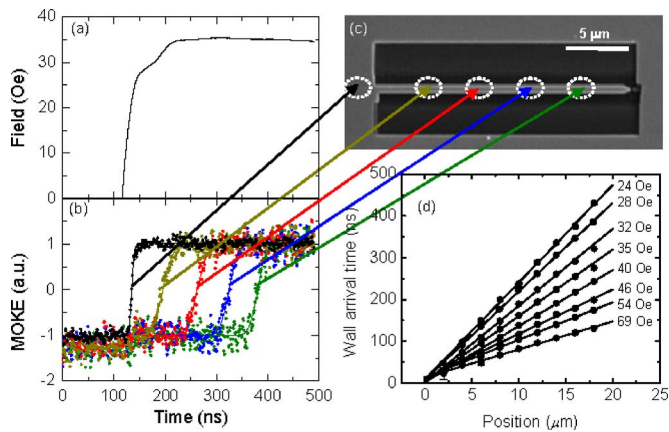


FIG. 8. Illustration of time-of-flight domain-wall velocity measurements. (a) Drive-field wave forms applied to drive a domain wall into and along a nanowire. Negative-going saturation pulse (not shown) preceded the positive-going field. (b) Time-resolved MOKE signal (symbols) and fits to the error function (solid lines), in response to the 35 Oe field wave form of (a). (c) The MOKE transients were measured at the nanowire locations indicated in the scanning electron micrograph. Ellipses approximate the  $1/e$  width of the laser spot (incident at  $45^\circ$ ). (d) Mean domain-wall arrival time vs position along the nanowire for different field-step amplitudes. The inverse slope of these wall trajectories yields the average velocity.

that wall into and propagate it along the nanowire. The time-resolved MOKE is probed at various locations along the nanowire, and the average domain-wall arrival time at each location is obtained from the averaged MOKE transients measured over many (several  $10^4$ ) reversal cycles to achieve sufficient statistics. These arrival time values versus position along the wire yield the mean domain-wall trajectory during reversal, and from these data the average wall velocity is determined.

Wall velocities ( $v$ ) are plotted versus field amplitude in Fig. 9, yielding the wall mobility curve. At the lowest fields,  $v$  increases linearly with  $H$  and peaks at a critical field  $H_p \approx 4.0$  Oe, above which  $v$  begins to decrease with increasing

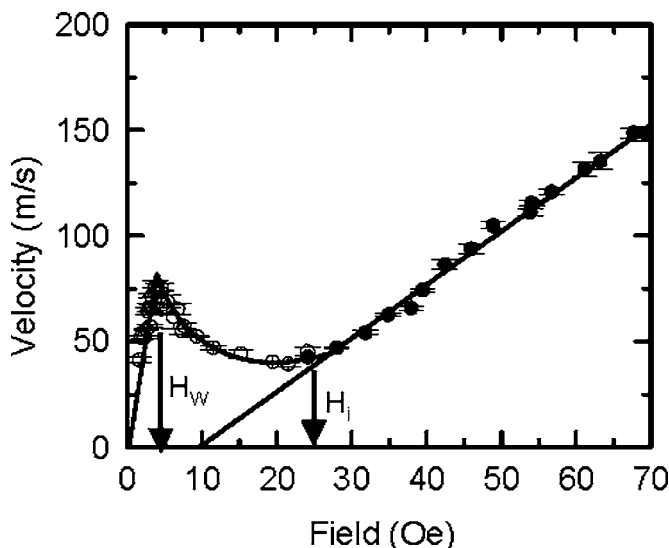


FIG. 9. Mobility curve (velocity vs field) for the nanowire shown in Fig. 8. The curve reveals a transition (Walker breakdown) from uniform domain-wall propagation (below velocity peak) to oscillatory propagation (above velocity peak).

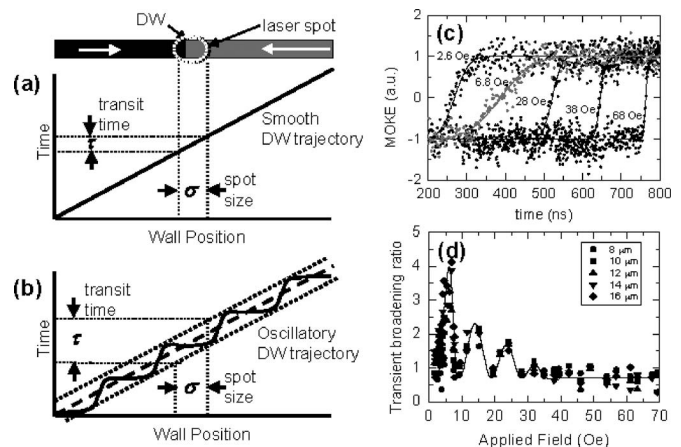


FIG. 10. Schematic illustration of the relation of the reversal transient width to the domain-wall velocity for (a) a uniformly propagating domain wall and (b) a domain wall moving with an oscillatory trajectory. (c) Reversal transients measured at a fixed location showing variation of width with field. The solid lines are fits to the error function. The transients for 6.8 and 2.6 Oe, just above and just below the critical field, respectively, have been shifted horizontally for clarity. (d) Ratio of the measured reversal transient widths to those expected for a domain wall moving at velocity  $v$  across a laser spot of width  $\sigma$ , where  $v$  is the average velocity shown in Fig. 9. Data are included for several measuring positions. The solid lines are visual guides.

$H$ . The negative differential mobility in this region gradually increases and becomes positive again above  $\approx 20$  Oe. For  $H > 30$  Oe the velocity-field characteristic regains linearity, but with a much lower mobility (slope). This mobility curve, described in more detail in Ref. 28, is one of the clearest experimental confirmations of a predicted dynamic transition termed Walker breakdown.<sup>29,30</sup> Above a critical field, the internal structure of the domain wall becomes unstable, causing a transition in wall propagation from smooth translation to an erratic, oscillatory propagation with reduced net average velocity.

This instrument has also provided evidence for the oscillatory dynamics predicted to occur above the breakdown transition, as described in Fig. 10. The spot profile has been measured (Fig. 2) and corresponds to a Gaussian. Therefore, the Kerr transient of a domain wall traversing the spot with a uniform velocity will assume an error function profile. A uniformly propagating domain wall with velocity  $v$  traverses the probe laser spot of width  $\sigma$  in a time  $\tau = \sigma/v$ . The transient width caused by a domain wall moving with an oscillating trajectory is different from the quantity  $\sigma/v_{av}$  expected from the average velocity obtained from wall trajectories such as in Fig. 8(d). If the phase oscillatory motion varies from cycle to cycle, the transient width is broadened by a convolution with the amplitude of the oscillation about the mean trajectory. If the phase is identical from cycle to cycle, the transient width is given by the average velocity of the wall as it crosses the spot, and that quantity will vary depending on the spot location and the spatial frequency of the wall oscillations. The measured reversal transient widths, compared to those expected from the average velocity, indicate that wall propagation above breakdown is nonuniform, in qualitative agreement with theory.<sup>29,30</sup>

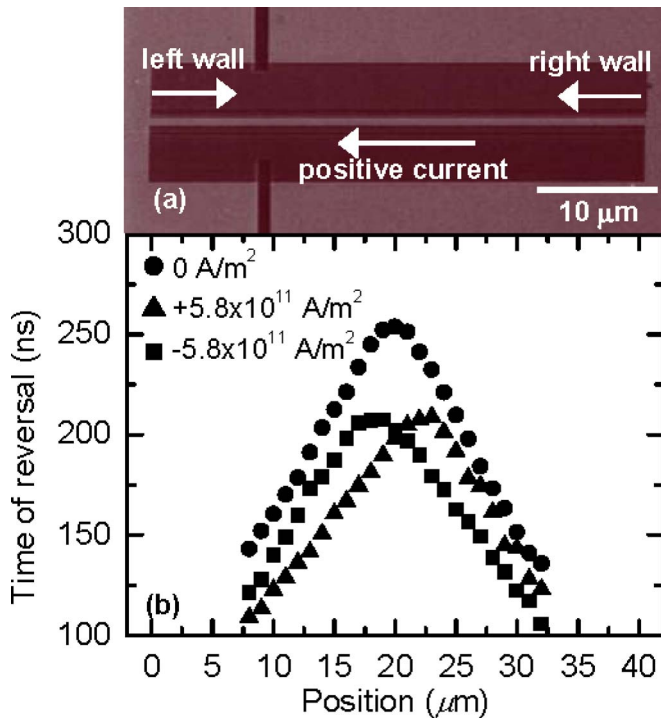


FIG. 11. (a) Scanning electron micrograph of device structure used for current-driven domain-wall motion studies: nanowire and contiguous large-area film regions (light contrast) and milled regions (dark contrast). The large-area regions at either end of the wire form electrically isolated contact pads for current injection. Directions of domain-wall propagation and positive current (opposite to direction of  $e^-$  flow) are indicated. (b) Average domain-wall trajectories during magnetic reversal under the application of a 40 Oe field step in the absence of current, and with injected current densities of  $j = \pm 5.8 \times 10^{11} \text{ A/m}^2$ .

### C. Current-driven domain-wall motion

The instrument has also permitted a systematic characterization of the dependence of domain-wall velocity on both field and current,<sup>22</sup> highlighting the similarities and differences between these two drive mechanisms. An example of these studies is described in Fig. 11. The 600-nm-wide thin-film Permalloy nanowire shown in that figure spans a milled trench that otherwise isolates two contiguous large-area film regions. The large film regions were used as domain-wall nucleation sources and as contact pads for dc injection. After the application of a field step, domain walls enter the wire at each end and propagate towards the center, as seen from the domain wall trajectories plotted in Fig. 11(b). Changes to the wall trajectories, and hence velocities, can then be studied as a function of dc (or pulsed current) injected into the nanowire and through the propagating walls. By exploiting the combined spatial and temporal resolutions of this instrument, changes in the propagation velocity of each individual wall can be monitored for any combination of field and current.

The velocity-current characteristic obtained for domain walls in the presence of a fixed field amplitude is shown in Fig. 12. These data are the first to cover a range sufficiently broad to ascertain the full functional dependence of the interaction of a current with a propagating domain wall.<sup>22</sup> The results confirm some features of recent theoretical descriptions, but find that the existing theoretical descriptions tell only part of the story. In addition to an established and intu-

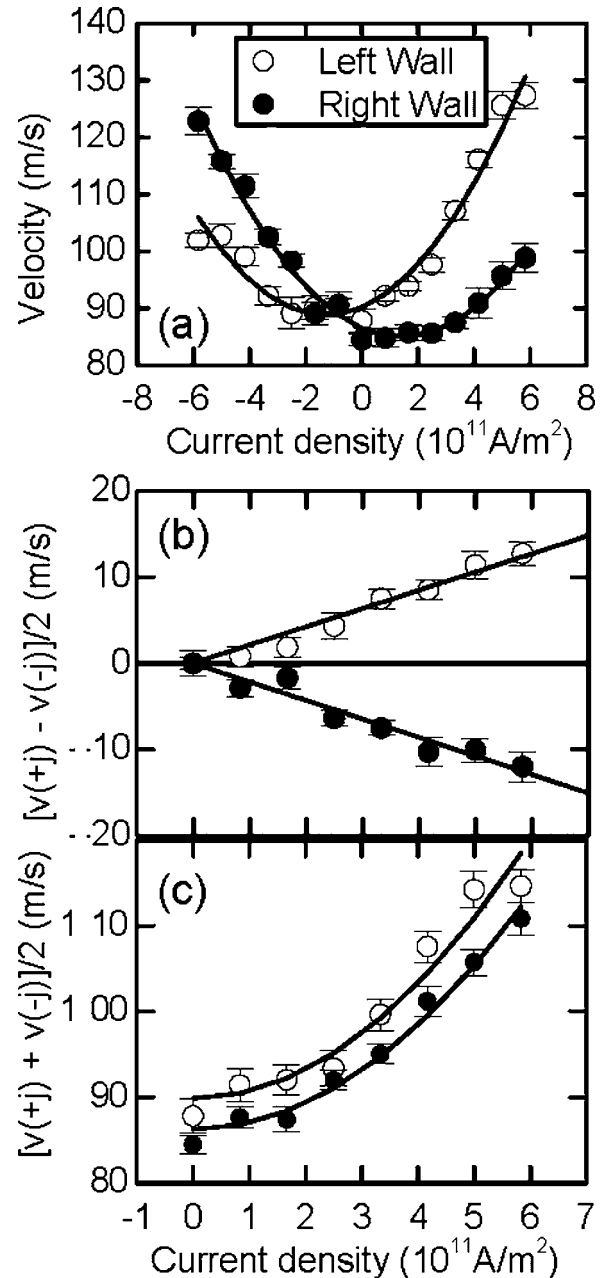


FIG. 12. (a) Wall velocity ( $v$ ) vs dc for leftward- and rightward-moving walls at an applied field  $H=47$  Oe. Existing spin-torque models predict a linear dependence between  $v$  and the current-density  $j$ . The measured response can be decomposed into its even and odd components about  $j$ , as shown in (b) and (c). The odd (linear) component agrees with the static “pressure” term of theoretical models, which would accelerate a wall traveling with the electron flow and decelerate a wall traveling against it. The even component, which tends to accelerate both walls regardless of the current direction, represents a new contribution of the spin torque to the wall-propagation dynamics related to the dynamic internal wall spin structure.

itively simple linear “spin pressure” on a domain wall in the direction of electron flow, there is a quadratic interaction that can accelerate a wall even if the wall is driven against the current by a magnetic field. The effect of this new interaction can exceed that of the first. This new phenomenon demonstrates that despite considerable theoretical efforts,<sup>18,31–33</sup> a full description of the spin-torque interaction is far from complete.

#### IV. SUMMARY AND DISCUSSIONS

A versatile high-speed, high spatial resolution MOKE polarimeter has been described. The instrument is capable of accurately measuring field- and electric-current-driven domain-wall motion in magnetic nanostructures at  $1\ \mu\text{m}$  spatial resolution and 1 ns temporal resolution. The instrument is also capable of measuring Barkhausen jumps, hysteresis loops, and frequency-dependent scaling of magnetic energy loss. Initial experiments carried out using the instrument have (1) clarified understanding of magnetic-loss scaling, (2) characterized field-driven domain-wall mobility in model 1D magnetic nanostructures, and (3) revealed a new nonlinear term in the electric-current (spin-torque) force driving domain walls at high current density.

#### ACKNOWLEDGMENTS

This work was supported by the NSF NIRT program (DMR-0404252) and the R. A. Welch Foundation (F-1015). Instrumentation was developed with support from the NSF IMR program (DMR-0216726) and the Texas Coordinating Board (ATP-0099). Device fabrication was performed using facilities of the Center for Nano and Molecular Science and Technology at UT Austin. Mobility experiments described in Sec. III were carried out in collaboration with M. Tsoi and C. Knutson. Microwave impedance measurements were performed with assistance from D. Neikirk and J. Kim.

<sup>1</sup> *Ultrathin Magnetic Structures*, edited by B. Heinrich and J. A. C. Bland, (Springer, Berlin, 1994).

<sup>2</sup> S. D. Bader and J. L. Erskine, *Ultrathin Magnetic Structures* (Ref. 1), p. 297.

<sup>3</sup> A. Hubert and R. Schäfer, *Magnetic Domains* (Springer, Berlin, 1998).

<sup>4</sup> T. J. Silva, C. S. Lee, T. M. Crawford, and C. T. Rogers, *J. Appl. Phys.* **85**, 7849 (1999).

- <sup>5</sup> A. B. Kos, T. J. Silva, and P. Kabos, *Rev. Sci. Instrum.* **73**, 3563 (2002).
- <sup>6</sup> A. B. Kos, N. R. Lopusnik, T. J. Silva, and Z. Celinski, *J. Appl. Phys.* **93**, 7068 (2003).
- <sup>7</sup> A. Y. Elezzabi and M. R. Freeman, *Appl. Phys. Lett.* **68**, 3546 (1996).
- <sup>8</sup> W. K. Hiebert, A. Stankiewicz, and M. R. Freeman, *Phys. Rev. Lett.* **79**, 1134 (1997).
- <sup>9</sup> G. M. Sandler, H. N. Bertram, T. J. Silva, and T. M. Crawford, *J. Appl. Phys.* **85**, 5080 (1999).
- <sup>10</sup> R. J. Hicken and J. Wu, *J. Appl. Phys.* **85**, 4980 (1999).
- <sup>11</sup> V. L. Safonov and H. N. Bertram, *J. Appl. Phys.* **85**, 5072 (1999).
- <sup>12</sup> B. C. Choi, M. Belov, W. K. Hiebert, G. E. Ballentine, and M. R. Freeman, *Phys. Rev. Lett.* **86**, 728 (2001).
- <sup>13</sup> P. Kabos, A. B. Kos, and T. J. Silva, *J. Appl. Phys.* **87**, 5980 (2000).
- <sup>14</sup> M. R. Pufall and T. J. Silva, *IEEE Trans. Magn.* **38**, 129 (2002).
- <sup>15</sup> M. R. Freeman and B. Choi, *Science* **294**, 1484 (2001).
- <sup>16</sup> D. A. Allwood, G. Xiong, M. D. Cooke, and R. P. Cowburn, *J. Phys. D* **36**, 2175 (2003).
- <sup>17</sup> S. Yang and J. L. Erskine, *Phys. Rev. B* **72**, 064433 (2005).
- <sup>18</sup> L. Berger, *J. Appl. Phys.* **55**, 1954 (1984).
- <sup>19</sup> P. P. Freitas and L. Berger, *J. Appl. Phys.* **57**, 1266 (1985).
- <sup>20</sup> M. Kläui, C. A. F. Vaz, J. A. C. Bland, W. Wernsdorfer, G. Faini, E. Cambril, and L. J. Heyderman, *Appl. Phys. Lett.* **83**, 105 (2003).
- <sup>21</sup> M. Tsoi, R. E. Fontana, and S. S. P. Parkin, *Appl. Phys. Lett.* **83**, 2617 (2003).
- <sup>22</sup> G. S. D. Beach, C. Knutson, C. Nistor, M. Tsoi, and J. L. Erskine, *Phys. Rev. Lett.* **97**, 057203 (2006).
- <sup>23</sup> I. F. Lyuksyutov, T. Nattermann, and V. Pokrovsky, *Phys. Rev. B* **59**, 4260 (1999).
- <sup>24</sup> H. J. Williams, W. Shockley, and C. Kittel, *Phys. Rev.* **80**, 1090 (1950).
- <sup>25</sup> C. Nistor, E. Farraggi, and J. L. Erskine, *Phys. Rev. B* **72**, 014404 (2005).
- <sup>26</sup> C. Nistor and J. L. Erskine (unpublished).
- <sup>27</sup> K. J. Sixtus and L. Tonks, *Phys. Rev.* **37**, 930 (1931).
- <sup>28</sup> G. S. D. Beach, C. Nistor, C. Knutson, M. Tsoi, and J. L. Erskine, *Nat. Mater.* **4**, 741 (2005).
- <sup>29</sup> N. L. Schryer and L. R. Walker, *J. Appl. Phys.* **45**, 5406 (1974).
- <sup>30</sup> A. P. Malozemoff and J. C. Slonczewski, *Magnetic Domain Walls in Bubble Materials* (Academic, New York, 1979).
- <sup>31</sup> C. Tataru and H. Kohno, *Phys. Rev. Lett.* **92**, 086601 (2004).
- <sup>32</sup> Z. Li and S. Zhang, *Phys. Rev. Lett.* **93**, 127204 (2004).
- <sup>33</sup> A. Thiaville, Y. Nakatani, J. Miltat, and Y. Suzuki, *Europhys. Lett.* **69**, 990 (2005).